7 Particle Physics with CMS

E. Alagöz, C. Amsler, V. Chiochia, C. Hörmann[7], H. Meyer, C. Regenfus, P. Robmann, J. Rochet, T. Rommerskirchen, T. Speer, S. Steiner, D. Tsirigkas[8], and L. Wilke

In collaboration with:
ETH - Zürich, Paul Scherrer Institut (PSI) and the CMS Collaboration

The main goal of the CMS experiment is to search for the Higgs boson and for physics beyond the Standard Model (SM). The mass of the Higgs can be calculated from the t-quark mass and radiative corrections: M_H <186 GeV (95% CL) (1). A light Higgs (M_H <130 GeV), decays mainly to $b\bar{b}$, a heavy Higgs mainly to four leptons via W^+W^- or Z^0Z^0. However, for light Higgs the $gg \rightarrow b\bar{b}$ background dominates the $H \rightarrow b\bar{b}$ signal in an inclusive search.

The Minimal Supersymmetric Standard Model (MSSM) is the most popular extension of the SM which stabilizes the Higgs mass and achieves unification at high energies. In addition to SUSY particles the MSSM requires five spin zero fields, the neutral h, H, A and the charged $H^{\pm}$. Two parameters (M_A and tanβ) are needed to fix their masses.

At pp colliders and for small tanβ the h, H, A should be produced dominantly by two gluons through the b- and t-quark loops (Fig. 7.1a) supplemented by SUSY contributions. However, large value of tanβ (≥ 5) are favoured (2) in which case the main Higgs production mechanism is radiation off b-quarks (Fig. 7.1b).

The h lies below 130 GeV and decays dominantly into $b\bar{b}$. The A and H decay into $b\bar{b}$ (or $t\bar{t}$), the H into hh for small tanβ which also lead to b-quarks. Hence the detection of B-mesons is of *crucial importance* in Higgs physics. Several benchmark channels for MSSM Higgs searches have been studied in CMS (3). The Zurich group is preparing a

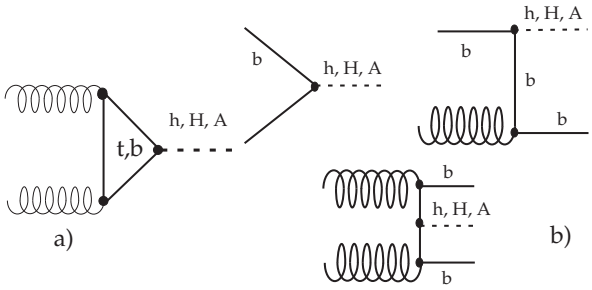

Figure 7.1: Main contribution to the MSSM Higgs production at the LHC for small tanβ (a). Higgsstrahlung becomes important for large tanβ (b).

search for the h associated with the decay of supersymmetric particles. However, during the first two years of LHC operation the luminosity will be well below the design value of 10^{34} cm^{-2}s^{-1} which makes an early discovery of the Higgs unlikely. Meanwhile tools (secondary vertex reconstruction, trigger, b-tagging) need to be developed or tuned with early data. We therefore plan to examine first b-physics issues, hence decays of B-mesons.

Many properties of the B_s, such as the differences between the masses and widths of the two weak eigenstates (B_S^H and B_S^L), can be studied with the decay $B_s \rightarrow (J/\psi)\phi$. A full reconstruction of the B_s can be achieved through the decays $J/\psi \rightarrow \mu^+\mu^-$ and $\phi \rightarrow K^+K^-$. First measurements of the mass difference Δm_s between B_S^H and B_S^L have recently been reported from the Tevatron (4). However, the difference between their widths, $\Delta\Gamma_s$, has not been measured with sufficient precision to be compared with the SM prediction ($\Delta\Gamma_s/\Gamma_s \sim 0.1$).

[7] Until June 2006
[8] CERN doctoral student

The $B_s \rightarrow (J/\psi)\phi$ decay also provides one of the best ways to determine the height of the unitarity triangle. One would measure the (CP-violating) asymmetry between $B_s \rightarrow (J/\psi)\phi$ and $\bar{B}_s \rightarrow (J/\psi)\phi$ which requires tagging the flavor of the B_s. An alternative method is to measure the angular distributions of the final state K's and μ's which are different for the CP-even and CP-odd components. This does not require tagging but large data samples which can be obtained at the LHC.

The Zurich group is contributing to the CMS experiment since 1995. We are involved in the reconstruction software, in particular track and vertex reconstruction (5; 6) and constraining kinematic fits (7). We are preparing the analysis of $B_s \rightarrow (J/\psi)\phi$ and a search for the MSSM Higgs bosons decaying into, or associated to, $\bar{b}b$ pairs. We are contributing to the innermost device, the barrel pixel detector, with which secondary vertices from B-decays can be determined. We have measured on CERN test beams the performance of pixel sensors before and after irradiation. Many details can be found in ref. (8). We have contributed to the development of the readout chip and of the power distribution system. We are constructing the mechanical support structure for the pixel detector and the service tubes which provide the coolant and power, and transfer the signals to and from the pixel detector.

7.1 Reconstruction software

In 2006 we ported the track and vertex algorithms (previously written in ORCA) to the new reconstruction environment (CMSSW) while maintaining the performance demonstrated in the Physics TDR (9). For the vertex reconstruction we had to rewrite the software and adapt the various fitters (Kalman, Gaussian-sum, and kinematic fits, see previous annual reports).

The CMS b-tagging working group, led by one of us (T.S.), is responsible for the development of b-tagging, offline vertex reconstruction algorithms and high level trigger (HLT) for b-decays. The main feature used to distinguish b-jets from light flavour jets is the long lifetime of B-hadrons. The simplest algorithm (used in the HLT) is based on the large impact parameter with respect to the primary vertex. More elaborate algorithms identify the b-decay vertex and select large decay lengths to reject the short-lived background. Further properties can be used, such as the large mass of the b-quark and the high (> 4) final state multiplicity.

The detection of an electron (or a muon) can be used, the semileptonic branching fraction of b-quarks to an electron being of the order of 10%. We are contributing to the reconstruction of electrons from semileptonic b-decays. Some b-jets contain electrons with follow curved trajectories in the magnetic field until they reach the electromagnetic calorimeter. Without tracker material the projection of the trajectories in the transverse plane would be circular, leading to energy deposits in the calorimeter extending over a small number of crystals. However, bremsstrahlung photons from the tracker material leads to azimuthal smearing of the energy deposits. We have improved on algorithms to disentangle energy deposits from different electrons and have included them in CMSSW.

7.2 $B_s \rightarrow (J/\psi)\phi$

This channel has been chosen a a benchmark channel by the CMS collaboration (3). In the offline analysis the decay $B_s \rightarrow (J/\psi)\phi \rightarrow \mu^+\mu^- K^+ K^-$ is reconstructed by combining a pair of $\mu^+\mu^-$ tracks with two additional tracks of opposite charges. As CMS does not possess a particle identification system all tracks have to be considered as possible kaon candidates. A kinematic fit is applied in which the

four tracks are constrained to a common vertex and the $\mu^+\mu^-$ invariant mass is constrained to the mass of the J/ψ.

A maximum likelihood fit of the decay angular distribution was performed on a sample of 14'000 simulated events, together with background events such as the dominant

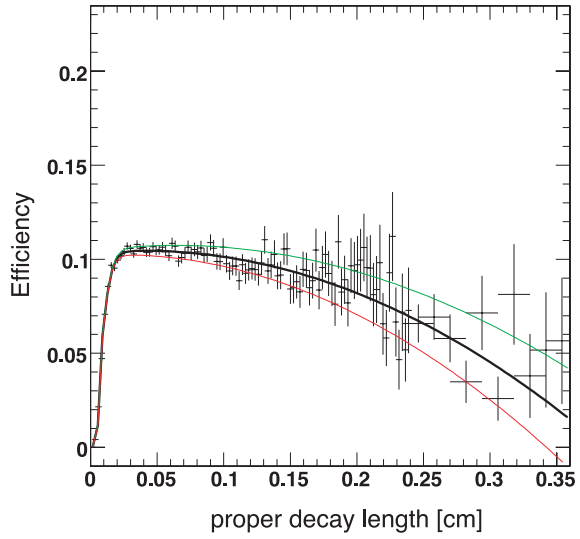

Figure 7.2: Distribution of the B_s-detection efficiency as a function of proper decay length with fit function and 1σ uncertainties.

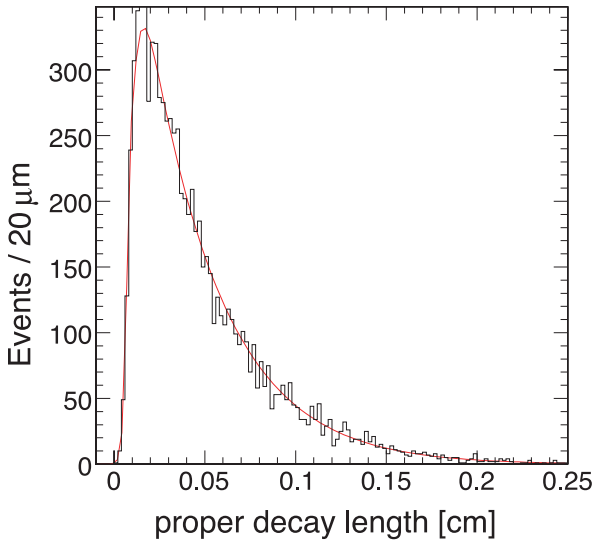

Figure 7.3:
B_s decay-length distribution with fit in red.

$B \to J/\psi X$. The decay $B_d \to J/\psi K^{*0} \to \mu^+\mu^- K^+\pi^-$ is of particular concern, since the pion can be confused with a kaon. This final state also displays a time-dependent angular distribution similar to that of B_s-decay. The modeling of the reconstruction efficiency for the decay length is delicate. Without appropriate correction the events at large decay lengths lead to shorter lifetime measurements (Fig. 7.2).

The analysis of $B_s \to (J/\psi)\phi$ assumes a HLT trigger to enrich the B_s-sample. (We are also developing a trigger for other b-channels such as $B_d \to J/\psi K^* \to \mu^+\mu^- K^+\pi^-$ or $B_s \to \mu^+\mu^-$). In a first step one searches for two muons in the CMS muon chambers with transverse momenta above 3 GeV/c. In the HLT b-candidates are identified through partial reconstruction of the decay products in restricted tracking regions. The muon tracks are then precisely reconstructed and the b-decay vertex determined. A minimum distance from the primary vertex is required and J/ψ events are selected by a cut on the 2μ-invariant mass. The efficiency of the trigger for $B_s \to (J/\psi)\phi \to \mu^+\mu^- K^+K^-$ events is 20%.

The resolution on the B_s-invariant mass after kinematic fit is 14 MeV and the resolution on the proper decay time 77 fs (7). The decay length distribution is shown in Fig. 7.3. The results show that we will be able to measure a value of say $\Delta\Gamma_s/\Gamma_s = 0.20$ with an uncertainty of 20%. To investigate the influence of $\Delta\Gamma_s$ on the measurement a simple Monte-Carlo simulation was developed which produces events according to the angular (time-dependent) distribution smeared with the experimental resolution. From these studies we conclude that the statistical error on $\Delta\Gamma_s/\Gamma_s$ will decrease to 5% for 110'000 events (corresponding to 10 fb^{-1}) at which point the systematic error will start to dominate.

7.3 $h \longrightarrow b\bar{b}$ in SUSY cascades

The lightest Higgs (h) can be produced in cascades between SUSY particle, e.g. $\tilde{\chi}_2^0 \rightarrow \tilde{\chi}_1^0 h$, $h \rightarrow b\bar{b}$, where $\tilde{\chi}_1^0$ is the lightest neutralino (possibly the WIMP of dark matter searches). These cascades start with the production of squarks and gluinos and can be identified through their comparatively large number of high energetic jets. In R-parity conserving supersymmetry the $\tilde{\chi}_1^0$ (with mass around 200 GeV) is stable. Since dark matter has survived until today, $\tilde{\chi}_1^0$ must be interacting only weakly with matter. Its signature in the CMS detector would therefore be a large missing energy. This signature offers a possibility to tag events for which the main decay mode $h \rightarrow b\bar{b}$ is otherwise hard to distinguish against QCD background. Previous studies showed that a 5σ discovery should be possible with 2 fb^{-1}(10) and thus a signal could be observed rather early at LHC. Efficient b-tagging algorithms are crucial to distinguish the b-jets in Higgs decay from those in other processes. Figure 7.4 shows an example of b-tagging efficiency based on PYTHIA and the CMSSW reconstruction software: as expected, efficient b-tagging also leads to a high background from lighter quarks.

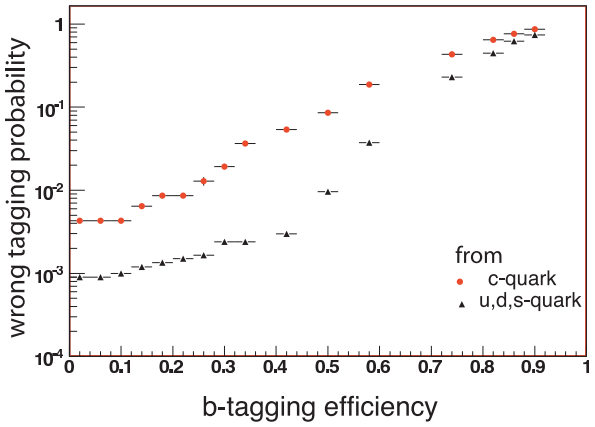

Figure 7.4: b-tagging efficiency vs. wrong tagging probability from c- or u-, d-, or s-jets.

7.4 Pixel sensors and associated software

The pixel barrel detector consists of three concentric cylindrical layers, 53 cm long, with radii of 4.4, 7.3 and 10.2 cm. The pixel sensors are made of n^+-structures on n-bulk silicon. They are mounted on segmented silicon plates connected by indium bump bonds to the readout chips. The analogue signals are read out to determine the coordinates more accurately, using charge sharing between pixels.

We have tested sensor prototypes with 105 – 225 GeV pions in the H2 beam line of the CERN SPS. Earlier results can be found e.g. in ref. (11) or in previous annual reports. In particular, we have demonstrated that the charge collection profiles measured in our beam tests and the expected trapping rates can be described by a two trap model producing a non-constant space charge density across the sensor bulk (12). This leads to electric field profiles with two maxima across the sensor bulk, one at each sensor edge. The model is supported by measurements of the electric field profile based on its dependence on the electron mobility. The measurements were obtained with a novel method using our test beam data (13). From these tests sensors with moderate p-spray isolation where chosen and the pixel size was fixed to 100×150 μm^2.

Our 2006 results on the position resolution are based on simulations relying on test beam data which were collected with pixels of dimensions 125×125 μm^2. The spatial resolution is improved after irradiation by applying so-called η-corrections to the charges collected on adjacent pixels (for details see our previous annual report). Figure 7.5 shows a simulation of the residual distribution (measured – predicted) for clusters of two pixels and tracks with an angle $\alpha = 20°$ with respect to the normal to the sensor surface. The sensor is assumed to have been irradiated with 5.9×10^{14}

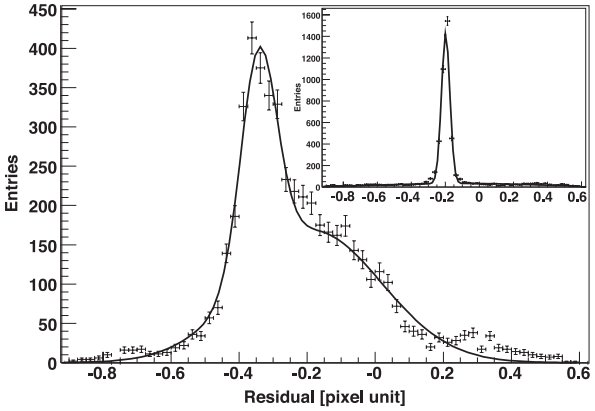

Figure 7.5: Distribution of residuals for incident tracks with α=20° and sensors irradiated to 5.9×10^{14} n$_{eq}$/cm^2. The continuous line is a double-Gaussian fit to the distribution. The inset shows the results with η-corrections. The residuals are not corrected for the Lorentz shift due to the magnetic field (from ref. [14]).

n_{eq}/cm^2, which corresponds to the first four years of LHC operation for the innermost layer. The distribution before correction is not described by a single Gaussian and is affected by large systematic errors which depend on the inter-pixel hit position. The width can be largely reduced by applying η-corrections (inset in Fig. 7.5). A position resolution below 15 μm can be achieved for perpendicular tracks in the CMS transverse plane (14), even after heavy irradiation. Table 7.1 summarizes the expected spatial resolution for perpendicular tracks and different irradiation fluences.

Another beam test was performed at CERN in 2006 with the final pixel sizes (100 × 150 μm^2)

Table 7.1:Expected position resolution for perpendicular tracks at various irradiation fluences Φ and bias voltages V_{bias}.

Φ [n_{eq}/cm^2]	V_{bias} [V]	Resolution [μm]
0	200	9.0±0.1
2×10^{14}	200	12.1±0.2
6×10^{14}	300	12.9±0.1

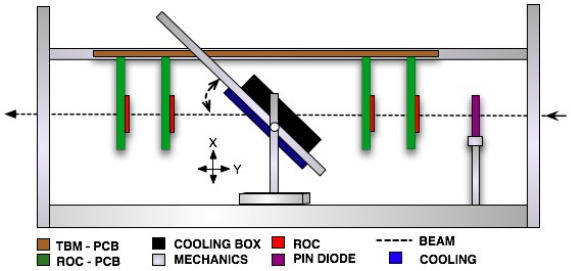

Figure 7.6: Setup used for our recent pixel test (see text).

and its front-end electronics in a 3 T magnetic field. Data were taken with irradiated and unirradiated pixel sensors with different chip calibration settings and bias voltages. The goal of this test was to study the position resolution of barrel pixel sensors before and after irradiation, with and without magnetic field, and to compare with expectations (Table 7.1).

The experimental setup (Fig. 7.6) consisted of a pixel sensor bump-bonded to a readout chip (ROC), a cooling device, a trigger system, a precise telescope to measure the direction of the incident pions, and a data acquisition system. The setup was located in a 3T Helmholtz coil with magnetic field perpendicular to the beam. The sensors (52 × 80 pixels)

Figure 7.7: PCB housing a pixel sensor bump-bonded to the ROC.

were bump-bonded to the ROC at PSI and irradiated at the CERN IRRAD1 facility with 24 GeV protons. The irradiation fluences varied from 0.37×10^{14} to $8.2 \times 10^{14} \mathrm{n_{eq}cm^{-2}}$. The irradiated samples were wire-bonded to a printed circuit board designed in our electronics workshop in Zurich (Fig. 7.7).

The beam telescope was made of four pixel sensor planes, bump-bonded to ROCs. Two of the planes were placed in front and two behind the test sensor. The beam telescope was used to determine accurately the hit position and incident angle on the test sensor. The planes were tilted by $20°$ to enhance charge sharing (and hence position resolution). The tested sensor was located in a cool box equipped with two cooling Peltier elements for operation at $-10°\mathrm{C}$. The hot sides of the Peltier elements were cooled with water and nitrogen gas was flushed in the cooling box to avoid condensation. The cooling box could be rotated for measurements at different incident angles. A trigger signal was provided by a 2×6 mm^2 PID diode which was synchronized to the SPS beam clock (40 MHz). The analysis of these data is in progress. Preliminary results indicate that the measured charge distribution and cluster multiplicity agree with expectations.

In 2006 we also used our two-trap model to develop new reconstruction algorithms and calibration procedures for irradiated pixel sensors. The drifting electrons experience the Lorentz force in the 4T field of CMS and drift perpendicularly to the magnetic and biasing electric field. Figure 7.8 shows the average charge collected in a pixel cluster as a function of distance from the track entry point. The figure is produced assuming 10 GeV muons at a pseudo-rapidity $\eta \sim 2$ and using the full CMS detector simulation. The Lorentz angle Θ_L can be extracted from this figure using the relation $\tan\Theta_L = \frac{L}{T}\tan\phi$ where L is the cluster length along the track direction and $T = 285$ μm is the sensor thickness. Figure 7.9 shows the effect from test beam data for comparison.

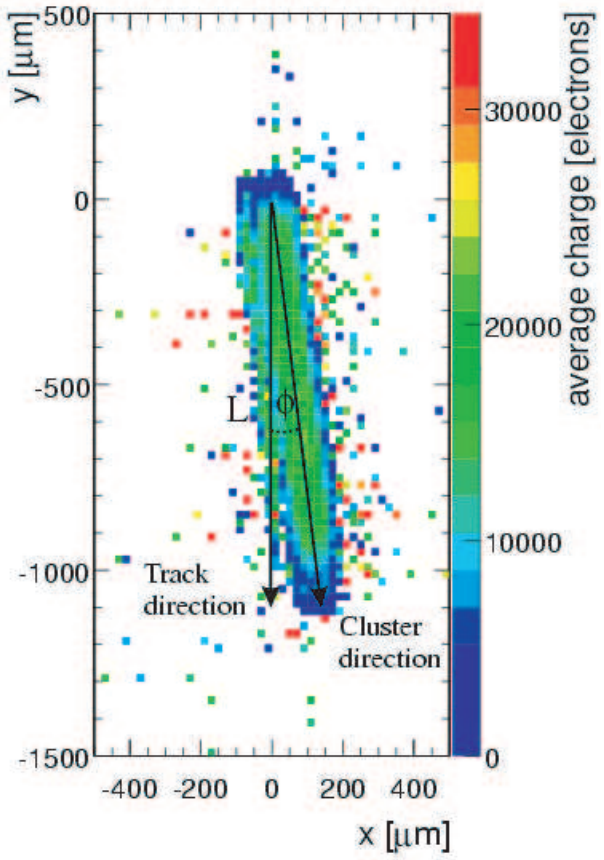

Figure 7.8: Average charge of clusters produced by 10 GeV muons in the first pixel barrel layer for η~2, as a function of distance from the track entry point (simulation). The y-coordinate is parallel to the beam direction. The collected charge is shifted along the x-coordinate due to the Lorentz effect.

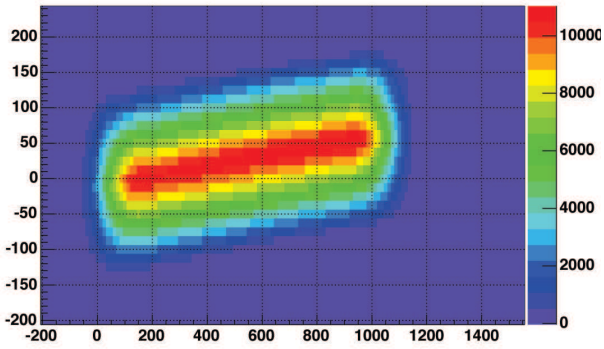

Figure 7.9: Real data from a beam test at 3 T.

Due to radiation damage the sensor response is expected to change during detector operation and several quantities have to be monitored to guarantee a precise determination of the hit positions. One of us (V.C.) is leading the pixel Data Quality Monitoring group (DQM). Data monitoring will be performed online and offline and includes raw hits, reconstruction of hit clusters and multiplicities, pixel track seeds, distribution of primary vertices from pixel tracks and impact parameters.

In particular, the Lorentz deflection leads to a shift of the hit coordinate (Fig. 7.5) which needs to be corrected. The correction (which can reach 120 μm) will change as a function of time and as a function of location due to radiation damages which modify the electric field distribution. The Lorentz angle will therefore be monitored in-situ. We wrote the software to extract the Lorentz deflection angle directly from CMS data. Since the three barrel layers will be exposed to different fluences, the Lorentz angle must be measured in each detector layer as a function of pseudo-rapidity. The shift can be determined for a given ionization depth in the sensor using a large number of well measured tracks (Fig. 7.10). The detector is subdivided into its

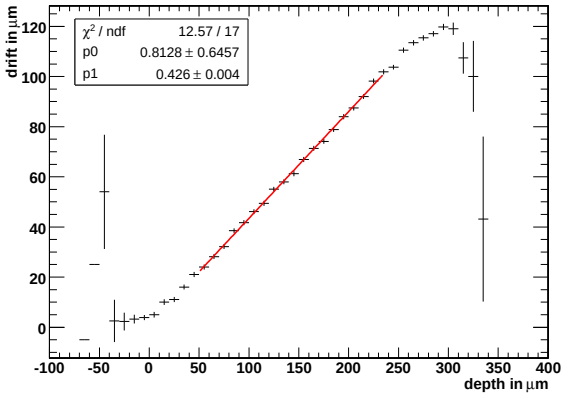

Figure 7.10: Shift of the hit coordinate due to the Lorentz drift as a function of depth at which the charge is produced in the sensor (simulation of non-irradiated sensors). The value for tan Θ_L is read from the slope of the fit (in red).

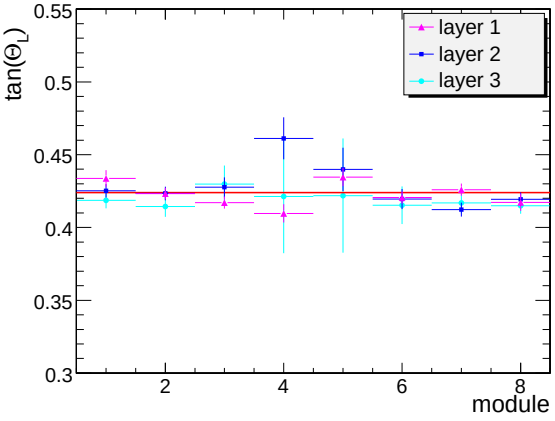

Figure 7.11: Reconstructed Lorentz angle angle for the 24 rings. The horizontal red line is the value assumed for the simulation.

three cylindrical layers with eight rings for various pseudo-rapidities. A separate fit is performed for each of the 24 rings. The reconstructed Lorentz angle from simulated $Z^0 \rightarrow \mu^+\mu^-$ events agrees with the assumed value in the simulation (Fig. 7.11).

We are currently developing applications for visualizing DQM histograms (web interface) and generate alarms. The DQM software will be tested with the pixel detector hardware during the integration phase planned for the first half of 2007.

7.5 Pixel efficiency

The performance of the barrel modules was studied in a recent PhD thesis (15). A module is made of 16 ROCs connected to the 66'560 pixels by the bump bonding technique. We measured the inefficiency under LHC conditions in a high rate pion beam at PSI and compared with simulations. The setup is shown in Figs. 7.12 and 7.12. The inefficiency is about 2% for the innermost layer (Fig. 7.14). Let us mention in particular the problem of Single Event Upsets (SEUs) which are due to the harsh radiation environment,

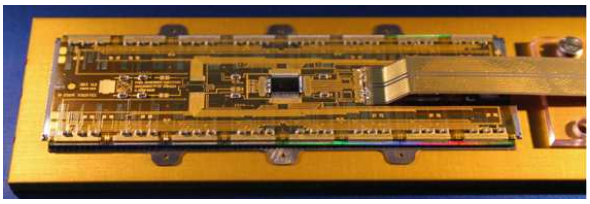

Figure 7.12: Pixel readout module.

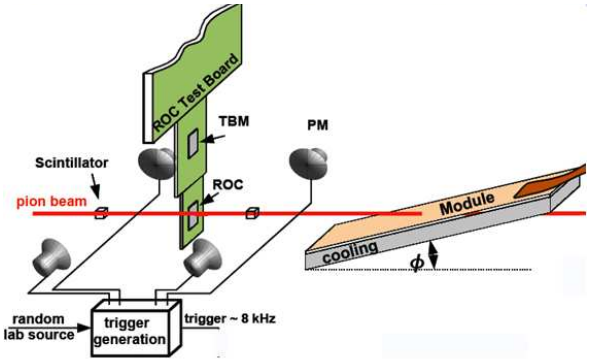

Figure 7.13: Beam setup to measure the inefficiency.

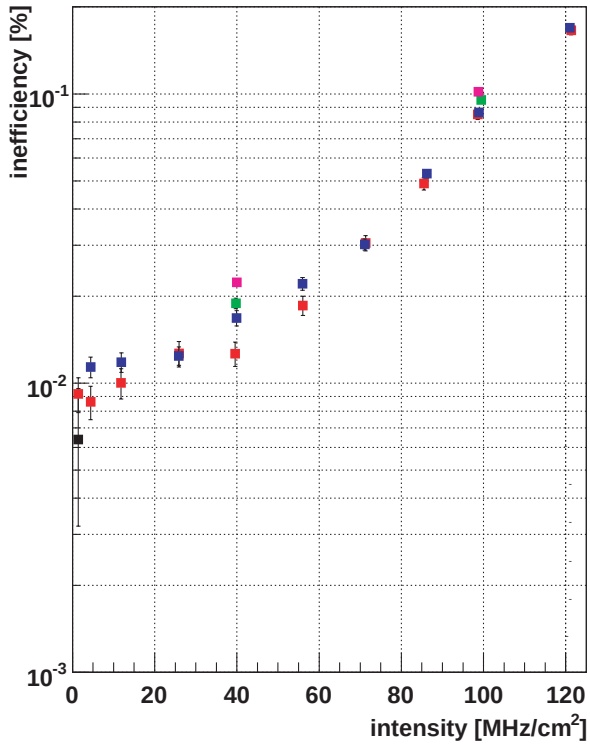

Figure 7.14: Inefficiency for different trigger rates (for details see ref. [15]). The flux at the innermost pixel layer in the LHC will be 60 MHz/cm^2.

causing corrupted memory cells. This was studied and alleviated with protection capacitors yielding about 1 SEU/s for the entire pixel barrel detector ($\sim 48 \times 10^6$ pixels) at full luminosity (15). This development is now completed and mass production is underway at PSI.

7.6 Detector support structure and service tubes

The support structure for the barrel pixel detector and the corresponding service tubes are currently under construction in the Institute's workshop. The 5m long assembly is made of two separated half shells containing the detector and two service half shells at each end (Fig. 7.15). The detector end-flanges were finalized in 2006 and adapted to the detector end-ring prints. The flanges consist of thin fibreglass frames (FR4) filled with foam (Airex) covered by carbon fibre blades. The end-flanges support the individual detector ladders of the three layers. The end-ring prints connect the detector modules mounted on the ladders to the readout electronics installed in the corresponding readout slots of the service tubes.

The various components, such as carbon fibre blades and cooling containers, were produced in 2006 and the assembly of the support structure has started. The power, the cooling fluid, the control and the optical signals are transferred through the service tubes to the pixel detector (Fig. 7.15). The massive cables are attached to the outer flange. The structure is supported by stainless steel tubes (wall thickness of 100 μm) connected to the stiffener rings and the inner and outer aluminium flanges. The tubes also supply the detector with the cooling fluid. The gaps are filled with Airex foam.

We have also designed the printed circuit supply boards (motherboards and readout elec-

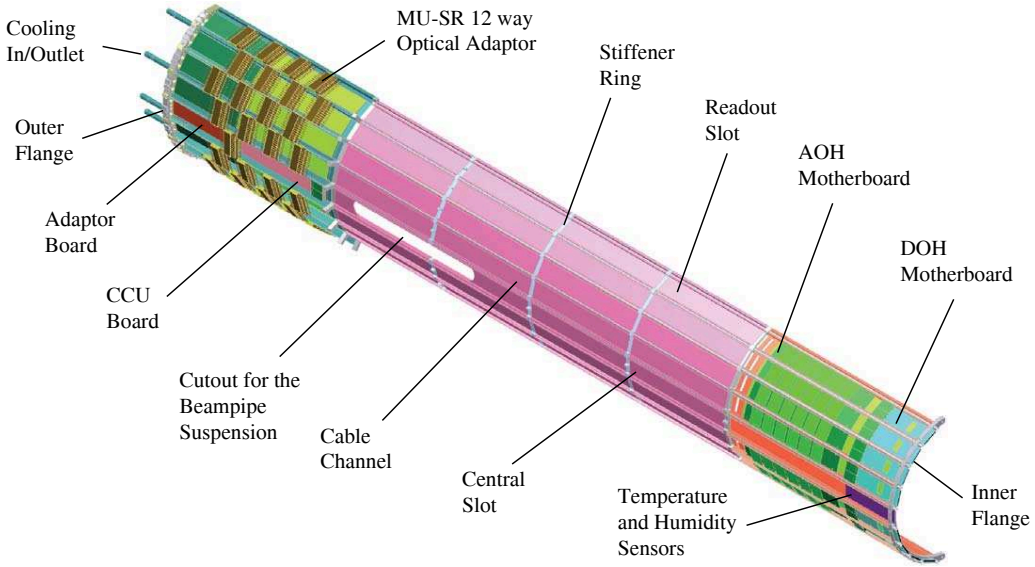

Figure 7.15: Overview of a supply tube half shell.

tronics). The motherboards which hold the optical hybrids for the analogue and digital control links are installed in eight readout slots near the detector on the integrated supply boards. The corresponding boards at the outer ends carry the power adaptor boards, which provide the detector power and the bias voltage. In the central slot the digital communication and control board (CCU) is installed which distributes the control signals to the individual readout boards of the eight readout sectors and collects the information on temperature, pressure and humidity. The optical fibres are loosely installed in the cable channels.

Our electronics workshop is involved in the pixel detector front-end control system. It consists of four CCUs, each controlling a quarter of the detector (eight barrel sectors). Figure 13.1 shows the block diagram of a CCU Board.

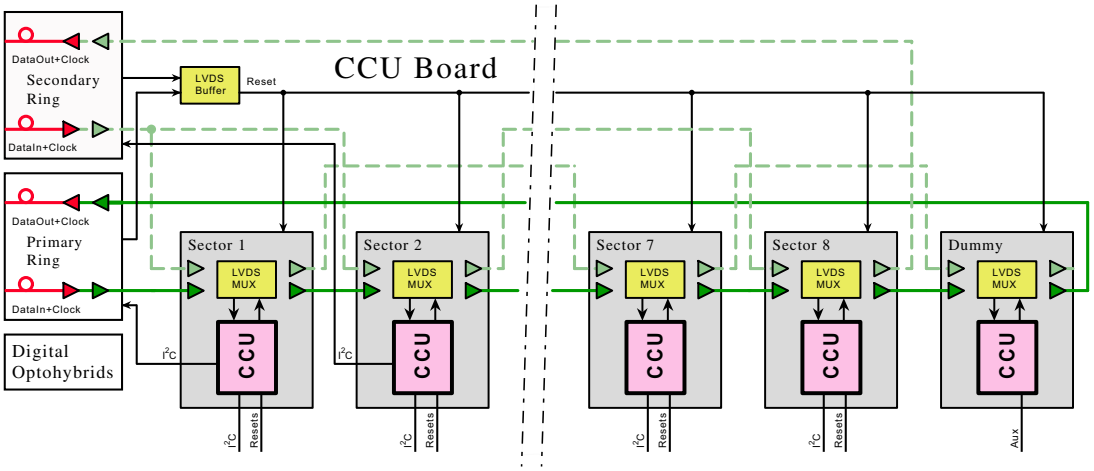

Figure 7.16: Block diagram of the Barrel Pixel control system. Only 5 of the 9 CCUs are shown for simplicity. One CCU board controls eight readout sectors of the barrel pixel detector.

Our group is also responsible for the design of the CMS pixel detector power distribution for the front end electronics (low voltage) and the pixel sensors (high voltage), and cabling. The power lines are integrated in the service tubes. The high and low DC voltages are generated with a commercial modular system manufactured by CAEN. The system has to cope with sudden (100 ns) current excursions of 2 A in 50 m long power lines.

The detector support structure for the three layers will be ready in August 2007 and the pixel detector will be installed in CMS in January 2008.

[1] LEP Electroweak working group (2005), http://lepewwg.web.cern.ch/LEPEWWG/ .

[2] For a brief summary, see C. Amsler, "SM and MSSM Higgs at the LHC", http://amsler.web.cern.ch/amsler/Higgs.pdf

[3] The CMS collaboration, "CMS Physics Technical Design Report Volume II: Physics Performance", CERN/LHCC 2006-021, CMS TDR 8.2, 2006.

[4] V.M. Abazov et al., Phys. Rev. Lett. **97** (2006) 021802; A. Abulencia et al., Phys. Rev. Lett. **97** (2006) 062003.

[5] R. Frühwirth and T. Speer, Nucl. Instr. and Meth. in Phys. Res. **A 534** (2004) 217.

[6] R. Frühwirth, K. Prokofiev, T. Speer, P. Vanlaer and W. Waltenberger, Nucl. Instr. Meth. in Phys. Res. **A 502** (2003) 699.

[7] K. Prokofiev, PhD Thesis, Universität Zürich (2005).

[8] Y. Allkofer et al., submitted to Nucl. Instr. Meth. in Phys. Res. **A**, prep. physics/0702092 (2007).

[9] The CMS collaboration, "CMS Physics Technical Design Report Volume I: Detector Performance and Software", CERN/LHCC 2006-001, CMS TDR 8.1, 2006.

[10] F. Moortgat, P. Olbrechts, L. Pape and A. Romeyer, CMS Note 2006/090.

[11] A. Dorokhov et al., Nucl. Instr. Meth. in Phys. Res. **A 530** (2004) 71.

[12] V. Chiochia et al., IEEE Trans. Nucl. Sci. **52** (2005) 1067; V. Chiochia et al., Nucl. Instr. Meth. in Phys. Res. **A 568** (2006) 51; M. Swartz et al., Nucl. Instr. Meth. in Phys. Res. **A 565** (2006) 212.

[13] A. Dorokhov et al., Nucl. Instr. Meth. in Phys. Res. **A 560** (2006) 112.

[14] E. Alagoz, V. Chiochia, M. Swartz, Nucl. Instr. Meth. in Phys. Res. **A 566** (2006) 149.

[15] C. Hörmann, PhD Thesis, Universität Zürich (2006).